Ultrasonics Sonochemistry 92 (2023) 106265

Contents lists available at ScienceDirect

Ultrasonics Sonochemistry

journal homepage: www.elsevier.com/locate/ultson

Hydrodynamic cavitation-enhanced photocatalytic activity of P-doped TiO_2 for degradation of ciprofloxacin: Synergetic effect and mechanism

Mengfan Chen, Kai Zhuang, Jiayi Sui, Congting Sun *, Youtao Song *, Nanxun Jin

College of Environment, Liaoning University, Shenyang 110036, PR China

ARTICLE INFO

Keywords:
Ciprofloxacin
Hydrodynamic cavitation
Hybrid AOP
Degradation mechanism
P-TiO_2

ABSTRACT

Hybrid methods with an enhanced oxidation capacity have been proposed for the removal of organic contaminants based on combining hydrodynamic cavitation (HC) with advanced oxidation processes (AOPs). In this study, we utilize the synergetic effect between photocatalytic processes and HC to strengthen ciprofloxacin (CIP) degradation by P-doped TiO_2 catalysts. In comparison to a degradation ratio of 20.37 % in HC and 55.7 % in P-TiO_2-based photocatalytic processes alone, the CIP degradation ratio reached as high as 90.63 % in HC-assisted photocatalytic processes with the optimal experimental parameters. The mechanic microjets treatment originated from HC make P-TiO_2 nano photocatalysts with significantly increased surface area, smaller particle sizes, cleaner surface and improved dispersion, which were found using SEM, TEM, and BET analysis. Possible degradation mechanisms and reaction pathways of CIP during hybrid HC + photocatalytic processes were explored by coupling free radical capture experiments and liquid chromatography-mass spectrometry . This hybrid HC + photocatalytic technique has a potential application in the treatment of antibiotic sewage at the industrial level.

1. Introduction

The demand and consumption of antibiotics in humans have been growing constantly due to an increase in population. Most antibiotics cannot be fully broken down and absorbed by humans or animals, and enter natural water bodies in unaltered forms through excretion in feces and urine [1,2]. Moreover, the overuse of antibiotics worldwide has been identified as the main driving force behind antimicrobial resistance [3]. O'Neill estimated that by 2050, increased antibiotic resistance (AR) could directly lead to 10 million deaths and about $100 trillion USD in financial losses worldwide [4]. Therefore, the development of a wastewater treatment method that can be effective and environmentally friendly for batch processing is essential.

Many physical and chemical methods are used for improving antibiotic degradation efficiency in wastewater. These include advanced oxidation techniques, biodegradation, adsorption, liquid extraction, and membrane techniques [5–9]. It has been demonstrated that the advanced oxidation processes (AOPs) are effective and have no significant limitations and problems in terms of secondary waste generation. AOPs can be used to effectively mineralize and degrade antibiotic pollutants. Currently, advanced oxidation techniques include ultrasound, Fenton, semiconductor photocatalysis, and ozonation [10]. Titanium dioxide (TiO_2) is a commonly used catalyst with the advantages of high stability, good performance, and easy preparation. However, the wide-band gap of TiO_2 leads to a weak ability to capture light. Moreover, the electrons and holes of TiO_2 can recombine together very quickly [11]. These shortcomings reduce the catalytic capability of TiO_2 in the redox reaction for degradation. Some improvement strategies have been proposed for TiO_2-based photocatalysts, such as metal and non-metal ion doping. This can increase the surface sensitivity, and create heterojunctions with other materials [12]. A common method for increasing photocatalytic activity is by doping non-metallic elements into TiO_2. These non-metallic dopants (e.g. N, P, S) can significantly narrow the band gap and improve degradation efficiency [13]. Compared to other non-metallic dopants, P has a closer ionic radius to Ti and only one valence state (P^{5+}), making Ti easily substituted by P in the TiO_2 lattice [14]. P dopants can inhibit the phase transition of TiO_2 from anatase to rutile, as well as build larger specific surfaces by suppressing the growth of anatase TiO_2. Feng et al. reported that P-TiO_2 catalysts present a higher removal efficiency of methylene blue than P25 and N-doped TiO_2 using ultraviolet and visible light [15]. However, the increased P content on the P-TiO_2 surface leads to an increase of surface acidity, which

* Corresponding authors.
E-mail addresses: congtingsun@lnu.edu.cn (C. Sun), youtaosong@sina.com (Y. Song).

https://doi.org/10.1016/j.ultsonch.2022.106265
Received 9 October 2022; Received in revised form 26 November 2022; Accepted 11 December 2022
Available online 13 December 2022

can cause long-term adsorption of contaminant molecules from the surface [16]. Further, due to the surface area limitation of P-TiO_2, the pollutant molecules attached to the surface may reduce the further degradation of the pollutant [17]. Wang et al. reported on the agglomeration of catalysts after photocatalytic reactions [18], which cannot be solved by non-metallic elements doping.

In large-scale industrial wastewater treatment, photocatalytic technology still has limitations due to long reaction times and the uneven particle size distribution of nano-catalysts [19]. Recent studies indicate that hydrodynamic cavitation (HC) technology has the advantage in easy operation and higher reaction energy, therefore, HC can serve as a potential approach for treating large amounts of sewage [20]. Wu et al. demonstrated that the cavitation intensity can be influenced by the liquid environment, pressure, and flow rate through the derivation of an approximate formula [21]. Thus, when the HC occurs, the rapid changes in the pressure and flow rate caused by the contraction of liquid can create different stages of cavitation intensity. Xu et al. found that the increase of fluid velocity can further enhance the reaction efficiency of cavitation by comparing experimental data with simulation effects [22]. The collapse of the cavity from downstream can create high temperatures (500–15000 K) high pressures (100–5000 atm) and strong shockwaves [23]. These extreme environmental factors can directly damage the structure of organic contaminants such as antibiotics in sewage [24]. Meanwhile, a significant amount of highly oxidizing reactive species have been found during the HC process. These radicals increase the removal efficiency of organic contaminants in sewage [25,26]. This can provide a promising hybrid oxidation technique by coupling photocatalysis with hydrodynamic cavitation. Similarly, Xu et al. designed oxidation experiments with potassium iodide to demonstrate the synergistic effect of cavitation and irradiation when performed simultaneously [27].

The process of HC shows unique advantages in treating antibiotic wastewater. The mechanical stirring in the photocatalytic process does not provide effective active substances for the degradation of organic macromolecules. However, a large number of free radicals can be formed in the HC process due to the energy generated by the expansion and collapse of cavities. Wu et al. confirmed the mechanism of expansion and collapse during HC [28]. For example, microjet, turbulence, and shear force can be produced during the HC process. These extreme conditions can well disperse photocatalyst particles and clean the surface of the catalyst for creating more active sites located on the catalyst surface and increasing the photocatalytic capacity of catalyst [29,30]. Moreover, as the bubbles burst in the HC process, UV light can be produced, which can enhance the electron/hole (e^-/h^+) pair production, generate hydroxyl radicals (•OH) by reducing dissolved oxygen and oxidize water molecules in water [31]. The addition of inorganic particles also increases the number of bubbles during the HC process. In the previous work, we used the hybrid method of Vis-UV + HC for the effective degradation of Rhodamine B [32]. Gogate et al. compared two different hybrid systems, via. HC and HC/UV/TiO_2 for degradation. A significantly higher degradation capacity of diclofenac sodium can be observed in HC/UV/TiO_2 process [33]. The degradation of tetracycline using HC and a photocatalytic process individually as well as a photocatalytic process coupled with HC was demonstrated by Wang et al. Results showed that almost 78.2 % degradation of tetracycline had been achieved by using P25 photocatalyst in combination results [18].

In this study, HC is used to activate P-TiO_2 to increase the specific surface area, expose more reactive sites, and replenish extra free radicals in order to assist the photocatalytic process for the removal of antibiotics. Ciprofloxacin (CIP) is one of the most widely used third-generation quinolone antibacterial drugs. CIP is selected to be used as a typical contaminant for investigating removal efficiency of the HC-assisted photocatalytic process with P-TiO_2. To further improve photocatalytic activity, P-TiO_2 photocatalysts were prepared with different P and Ti molar ratios by a simple sol–gel method. A venturi tube with optimal geometric parameters (discussed in the previous work) is used as the cavitation device. The operation parameters (inlet pressure, initial pH of solution, and initial concentration) are also investigated. In addition, the possible mechanism of HC-assisted photocatalysis under P-TiO_2 incorporation was also explored based on the characterization of the nanoparticles before and after the reaction.

2. Materials and methods

2.1. Chemicals

Ciprofloxacin (CIP, 98 %, AR) was commercially available from Shanghai Macklin Biochemical Co, ltd. Phosphoric acid (H_3PO_4, 85 %, AR) and tetrabutyl titanate ($Ti(OBu)_4$, $C_{16}H_{36}O_4Ti$, AR) were also purchased from Shanghai Macklin Biochemical Co, ltd and Damao Chemical Reagent Factory. The sodium hydroxide and hydrochloric acid were both purchased from Shanghai Sinopharm Chemical Reagent Co. (China) without further purification. Isopropanol (IPA), potassium iodide (KI), and 1,4-benzoquinone (BQ) were utilized for the trapping experiment. The aqueous liquid was prepared in DI water. The chemicals involved in this work were of analytical grade without further treatment and purification.

2.2. Pure and P-doped TiO_2 synthesis

The pure and P-doped TiO_2 nanoparticles were synthesized by a hydrolysis reaction between tetrabutyl titanate and an aqueous solution of phosphoric acid using a previously reported method with minor modifications [34]. Firstly, acetic acid and $Ti(OBu)_4$ were dissolved in ethanol (C_2H_5OH) under stirring. After 30 min of stirring, phosphoric acid was slowly added to the mixture in different proportions and was allowed to keep stirring for an additional 3 h until a milky white sol was obtained. A gel was obtained after aging for 12–24 h. The gel was then dried at 100 °C and calcined in a muffle furnace for 2 h at 550 °C. In this work, P-TiO_2 particles were synthesized at molar ratios of 0.02, 0.04, and 0.06 (P/Ti) and were labeled as P-TiO_2-0.02, P-TiO_2-0.04, and P-TiO_2-0.06.

2.3. Characterization of catalysts

The crystal phase of the prepared nanoparticles was investigated using X-ray diffraction (XRD, Bruker D8, Germany). An F-2500 spectrophotometer was used to measure the photoluminescence (PL) spectra at an excitation wavelength of 398.0 nm. A UV–vis spectrophotometer (Shimadzu, UV-3600, Japan) was used to record the UV-vis diffuse reflectance spectrum of the samples. X-ray photoelectron spectroscopy (XPS, EscaLab 250Xi, USA) was utilized to measure the surface electronic behavior. Scanning electron microscopy (SEM, Hitachi SU8000, Japan) was used to characterize the morphologies and microstructures of particles. A Malvern Zetasizer Nano ZS90 was used to measure the zeta potential for determining the point of zero charge (pHPZC) of the samples. The BET surface area was measured by a surface area analyzer (Quantachrome, Autosorb iQ, USA). The EPR spectroscopy was utilized to identified the active species using a Bruker A300-10/12 spectrometer.

2.4. Design of the experimental reactor

The schematic for the synthesis of P-TiO_2 and the experimental process is shown in Fig. 1a. The HC + photocatalytic experimental equipment is illustrated in Fig. 1b. The equipment worked as a closed-circulation unit, where contaminated liquid was circulated from a thermostatic water container through PPR pipes (inner diameter: 15 mm) into a cavitation generator (slit venturi) by a self-priming pump (Rili pump, WZB-1500A, Japan) with 1.5 kW power. The temperature of the contaminated liquid was controlled and maintained by a thermostatic water container at 25 ± 5 °C. The inlet pressure and flow rate were monitored by a pressure gauge and a flow meter in the main line. The

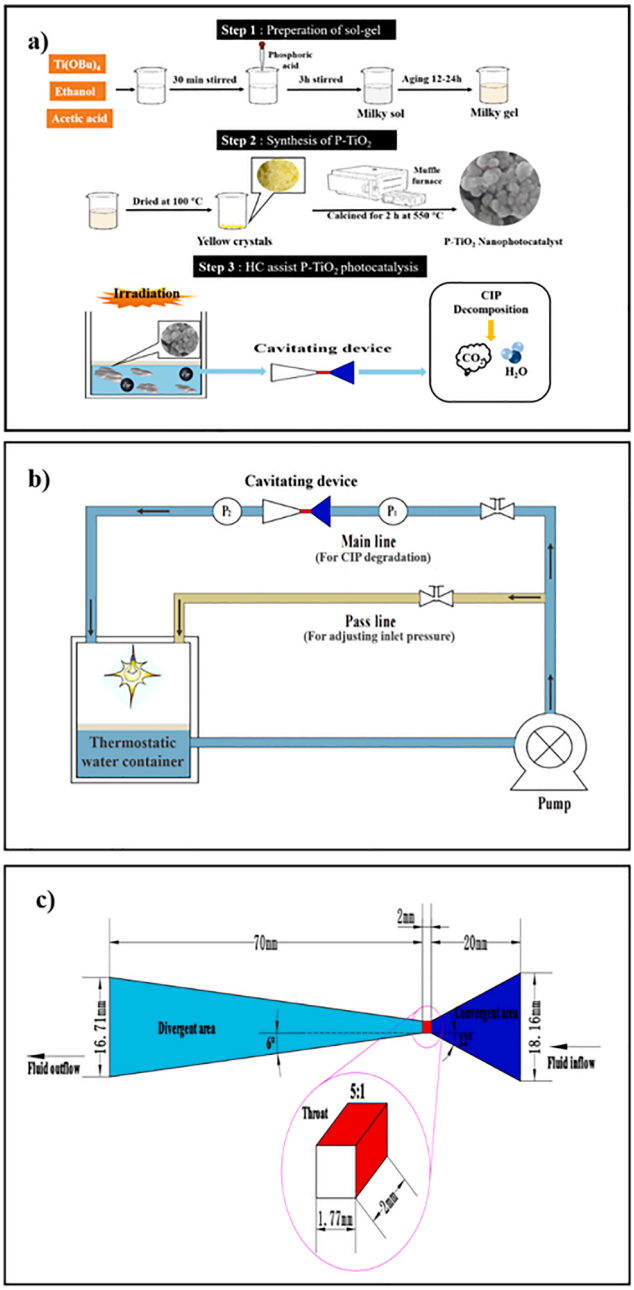

Fig. 1. (a) Schematic for the synthesis of P-TiO_2 and the experimental equipment (b) of individual and combined processes of HC and photocatalysis and geometric parameters (c) of used square venturi.

inlet pressure in the main line was regulated by a bypass line. All the irradiation-related experiments were carried out under a Xenon-lamp, loaded above the water surface in the thermostatic water container. Fig. 1c shows the geometric parameters of the square venturi. The hybrid advanced oxidation process can be realized by coupling Xenon-lamp irradiation with a cavitation generator in the experimental equipment. The optimal geometric parameters for square venturi have been discussed in our previous studies [32].

2.5. Experimental details

The related HC, photocatalysis, and HC + photocatalysis experiments to study the degradation efficiency of CIP were all done using the setup shown in Fig. 1. All the batch experiments were performed using 5L of CIP in an aqueous suspension. Photocatalytic batch experiments were done with a catalyst dose of 0.5 g L^{-1} and an initial pH value in the range of 3 to 11. Three different CIP concentrations (5, 10, 15 mg L^{-1}), and P/Ti molar ratios of 0.02, 0.04, 0.06 were tested. The temperature of reactant mixture was maintained at 30 °C. For the HC batch experiments, the initial conditions were 10 mg L^{-1} of CIP aqueous suspension with an initial operating pressure from 3 to 5 bar and an initial pH of 7. Before the HC treatment, the sample achieved catalyst-substrate equilibrium in darkness.

The HC + photocatalytic CIP removal experiments were carried out with a Xenon-lamp placed above the thermostatic water container and 3 bar HC operation pressure. The P/Ti ratio, pH, and initial CIP concentration were optimized and used in the HC + photocatalysis process. The response mixture was mechanically stirred in darkness for half an hour to reach catalyst-substrate equilibrium. The P-TiO_2 nanoparticles achieved catalyst-substrate equilibrium in darkness before HC + photocatalytic treatments.

2.6. Analytical methods

The UV–vis absorbance was measured at 277 nm for each collected sample. Sample concentrations were calculated using a calibration curve made using the CIP stock solution. The ratio of CIP removal was calculated by the following equation:

$$\text{Degradation ratio } (\%) = \frac{[C_0 - C_t]}{C_0} \times 100\,\% \quad (1)$$

where C_t is the instant CIP concentration and C_0 is the initial CIP concentration.

The intermediates during CIP removal were determined by HPLC-MS using a Shimadzu LC/MS-8050. Separation was done using a C-18 column (250 mm × 3.5 mm, 5 μm). The flow rate and injection volume of HPLC-MS separations were 1.5 mL min^{-1} and 2 μL, respectively. The composition of the mobile phase was 30 % methanol and the pH of the liquid was adjusted by formic acid.

3. Results and discussion

3.1. Characterization of nanoparticles

Fig. 2a illustrates the XRD patterns of pure TiO_2 and P-TiO_2 synthesized at 550 °C. As seen from the XRD patterns, the main peak of all samples appeared at 2θ = 25.27° with the other diffraction peaks appearing at 37.95°, 48.05°, 54.03°, 55.06°, 62.84°, and 69.1°, respectively. These peaks can be compatible with the crystal planes of (1 0 1), (0 0 4), (2 0 0), (1 0 5), (2 1 1), (2 0 4), and (1 1 6) for anatase TiO_2 (JCPD #21–1272). The diffraction peaks of samples are sharp and no impurity peaks derived from other TiO_2 phases have been found. The results demonstrate that P doping has no effect on the crystalline phase of TiO_2. The (1 0 1) peak of P-TiO_2 becomes broader and smaller with increasing P-doping concentration (Fig. 2b), which is consistent with previous reports [35]. This may be caused by a partial substitution between Ti^{4+} (0.35 Å) and P^{5+}, which has a larger ionic radius (0.68 Å), resulting in local lattice distortion. Moreover, the decreased peak intensity indicates that doping P^{5+} may reduce the crystallinity of TiO_2.

For semiconductor photocatalysts, the recombination ability of photo-generated carriers plays a critical role in improving their photocatalytic activity. PL spectroscopy was utilized to measure the ability for the recombination of e^-/h^+ pairs for as-prepared TiO_2 catalysts. Fig. 3 shows the PL spectroscopy of pure phase TiO_2 and P-TiO_2 nanoparticles (P/Ti = 0.02, 0.04, 0.06). The four samples show a wide emission band in the range of 350 ~ 600 nm (λ_{ex} = 398 nm). The PL intensity of P-TiO_2 is lower than that of pure TiO_2, indicating that the doping of P^{5+} causes a significant reduction in the recombination of e^-/h^+ pairs. The PL intensity of P-TiO_2 nanoparticles depends on the P/Ti molar ratio, whereby P-TiO_2-0.04 has the lowest PL intensity. This is consistent with

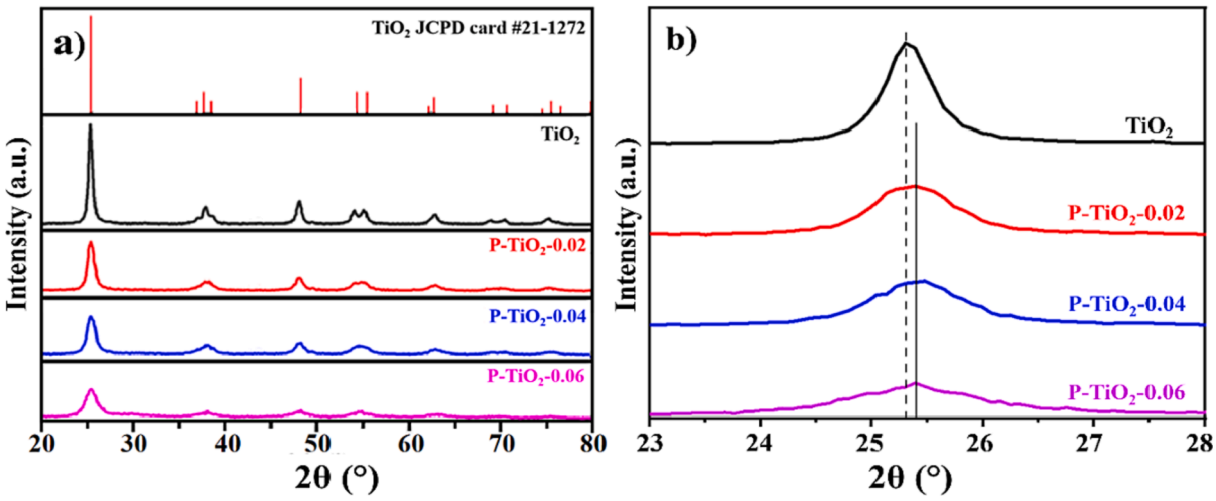

Fig. 2. (a) XRD patterns of pure TiO_2 and P-TiO_2 nanoparticles, (b) (1 0 1) XRD peak positions of the anatase for pure TiO_2 and P-TiO_2 nanoparticles obtained with different P/Ti.

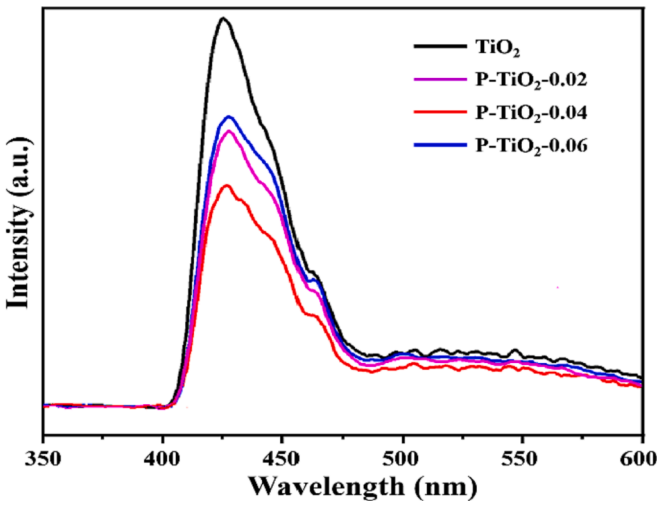

Fig. 3. PL spectra of pure phase TiO_2 and P-TiO_2 nanoparticles (P/Ti = 0.02, 0.04, 0.06).

Bai's previous study [36]. The higher P dopant concentration will cause excessive oxygen around phosphorus, which will form an electron trap and hinder electron-hole pair recombination in P-TiO_2-0.04.

Furthermore, the optical response of nanoparticles was investigated using diffuse reflectance spectroscopy (DRS). P dopants can significantly affect the optical absorption of TiO_2 (Fig. 4a). The addition of P significantly expands the absorption edge from 390 nm to the range of 410 ~ 440 nm, showing a red shift [37]. Notably, a blue shift in the absorption edge of P-TiO_2 occurs when the P/Ti ratio increases above 0.04. The results show that the doping of P evidently improves the absorption of visible light. The TiO_2 catalyst with a P/Ti ratio of 0.04 has the strongest absorption of visible light and enhances the photocatalytic removal efficiency of organic pollutions. The Kubelka-munk function was utilized to calculate the value of the band gap energy [38]. According to Fig. 4b, the band gap energy of pure TiO_2 is estimated to be 3.12 eV, which is consistent with the previous work [39]. Xu et al. have shown the existence of a critical concentration of P which minimizes the leap energy and maximizes the solar energy absorption of P-TiO_2 [40]. Our results illustrate that the band gap of P-TiO_2-0.04 (estimated as 2.86 eV) is smaller than that of P-TiO_2-0.02 (2.99 eV) and P-TiO_2-0.06 (3.02 eV), agreeing with Xu's work. Therefore, the P-TiO_2-0.04 sample would exhibit a better photocatalytic activity than the other samples. In the following discussions, P-TiO_2-0.04 was selected to compare with pure TiO_2 in order to demonstrate the advantages in surface chemical states and microstructures.

The XPS data were utilized for the analysis of the chemical states and composition of elements carried out on P-TiO_2-0.04. The synthesis of P-TiO_2 is shown in the XPS spectrum of Fig. 5(a), and Fig. 5(b)-(d) illustrates high characteristic peaks of Ti 2p, O 1s, and P 2p [14]. From Fig. 5b, the Ti 2p spectra of P-TiO_2 is accompanied by two satellite peaks centered at 459.2 eV and 465.1 eV, attributed to Ti $2p_{1/2}$ and Ti $2p_{3/2}$.

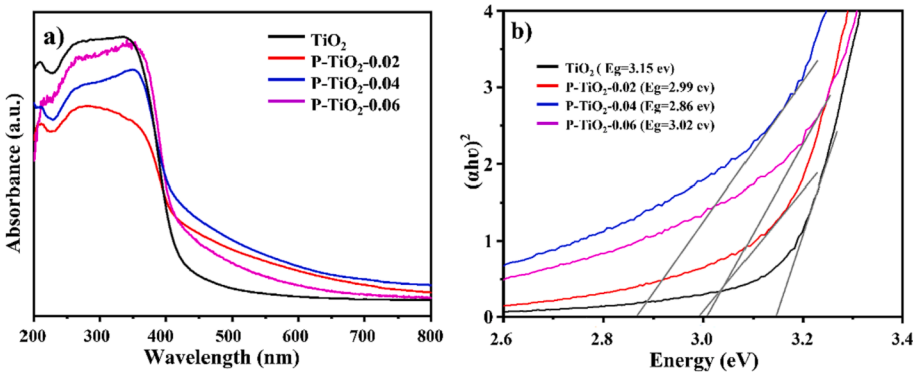

Fig. 4. UV–vis DRS spectra (a) and calculated corresponding band-gaps (b) of P-TiO_2 nanoparticles with different P/Ti molar concentrations (P/Ti = 0, 0.02, 0.04, 0.06).

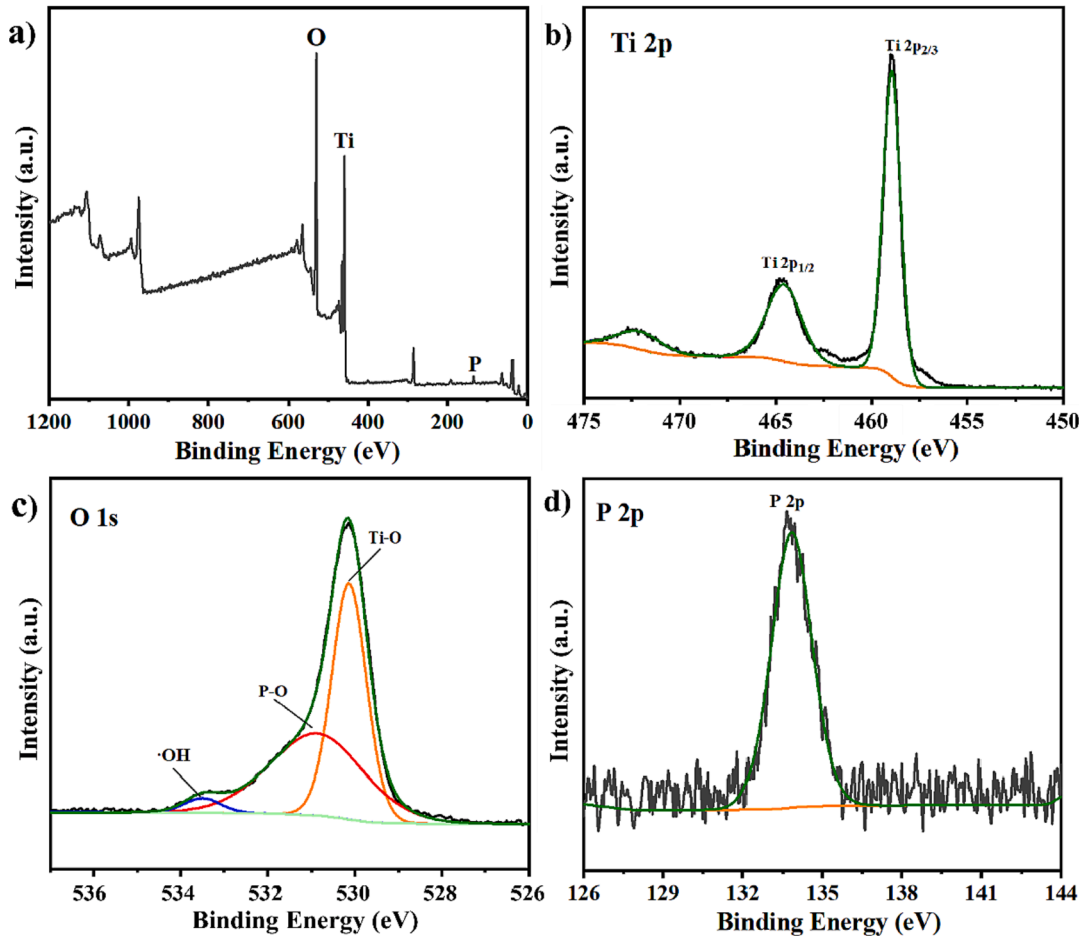

Fig. 5. The XPS full spectrum of P-TiO_2-0.04 (a)and high resolution XPS spectra of Ti 2p (b), O 1s (c) and P 2p (d).

Moreover, three peaks around 530.1 eV, 531.1 eV, and 533.5 eV in O 1s spectra (Fig. 5c) correspond to the Ti-O bond, P—O bond and ·OH, respectively [41]. Compared with the previous XPS spectra of pure TiO_2 [36], the O 1s core level at 530.1 eV for P-TiO_2-0.04 implies that P was incorporated into TiO_2 lattice by substitution of Ti atoms rather than interstation of Ti—O—P. The peak at 133.9 eV belongs to P $2p_{2/3}$

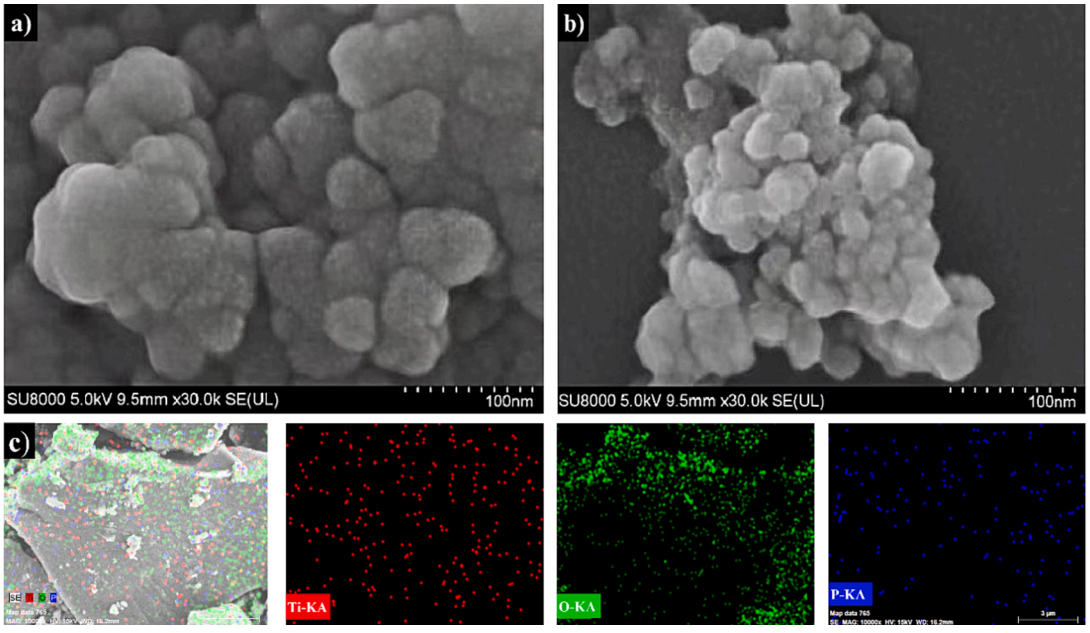

Fig. 6. SEM image of (a) pure TiO_2, (b) P-TiO_2-0.04, and (c) the corresponding SEM-EDX mapping images in the selected area of the P-TiO_2-0.04 nanocatalyst, respectively.

(Fig. 5d), indicating the presence of P^{5+} in the P-TiO_2-0.04 [42]. The XPS results verified the successful synthesis of a P-doped TiO_2 photocatalyst.

The microstructure of pure TiO_2 and P-TiO_2-0.04 nanoparticles were characterized by SEM. Fig. 6 depicts the prepared TiO_2 and P-TiO_2 nanoparticles showing approximately spherical morphology with different sizes. The particle size of pure TiO_2 (~650 nm average diameter) was found to be more regular and larger than that of P-TiO_2 (~450 nm average diameter), indicating that the growth of TiO_2 is inhibited by the P dopant. Moreover, doping P into TiO_2 can also improve the dispersion of nanoparticles. As shown in Fig. 6c, SEM-EDS elemental mapping displays that the elements of Ti, O, and P are well scattered on the surface of P-TiO_2-0.04.

Characterization and comparison of the textural properties of TiO_2 and P-TiO_2-0.04 photocatalysts was done using N_2 adsorption/desorption isotherms. The isotherms of the fabricated photocatalysts are determined as type IV with an H_3 hysteresis loop according to IUPAC [43], indicating mesoporous properties. Moreover, the BET surface area of P-TiO_2-0.04 (Table 1) is 1.5 times higher than that of pure TiO_2. The multi-point BJH method was used to measure the pore size of pure TiO_2 and P-TiO_2-0.04. As shown in Fig. 7b, P-TiO_2-0.04 has a smaller pore size, which is confirmed with SEM results. In summary, P dopants provide a larger SET surface and smaller pore size, which could expose more active sites and guarantee better adsorption and photocatalytic activity.

3.2. Photocatalytic degradation of CIP

Fig. 8a shows the influence of the P/Ti mole ratio on CIP photocatalytic degradation. The time profile of CIP degradation is fitted to pseudo 1st order kinetics by the formula:

$$-\ln(C/C_0) = kt \quad (2)$$

where C and C_0 are refer to initial and final concentrations of CIP (mol L^{-1}), k is the rate constant (min^{-1}) and t is the time of process.

The degradation efficiency of CIP first increased and then decreased with increasing P/Ti ratio from 0 to 0.06. The fact that degradation efficiency depends on P/Ti ratio can be attributed to the effects of P doping on mediating the photocatalytic activity of TiO_2. Both our present work and pervious works [44–46] have observed a P dopant concentration dependence for the photocatalytic activity of TiO_2. The doping of P element can increase the oxygen content on the surface of TiO_2 [44]. When the oxygen around phosphorus is excessive, it will cause electron trap formation and hinder the compounding of electron-hole pairs [45]. Meanwhile, P^{5+} replacing Ti^{4+} in the anatase TiO_2 lattice can promote the absorption of visible light by TiO_2 [46], thus improving the photocatalytic effect. It is notable that there exists a critical P doping concentration for achieving the maximum absorption of solar light. Previous DFT calculations explain that once the doping level is higher, the optical energy gap of photoexcitation is blue shifted as a result of the upshift of the Fermi level that is located deep inside the conduction band [46]. In our present work, the P/Ti = 0.04 acts as the critical value. Particularly, with the increasing P/Ti from 0 to 0.04, the bandgap energies of P-TiO_2 reduced from 3.15 eV to 2.86 eV. By further increasing P/Ti to 0.06, the bandgap energies of P-TiO_2 was 3.02 eV (Fig. 4b), agreeing with theoretical results [46]. The bandgap narrowing facilitates the improvement of visible light absorption. Therefore, the degradation efficiency first increased and then decreased with increasing P/Ti ratio. Furthermore, a maximum degradation efficiency of 55.7 % was achieved using P-TiO_2-0.04 under light irradiation for 120 min indicating that the P-TiO_2-0.04 showed the highest photocatalytic activity. This can be attributed to a wider absorption range of light, narrower bandgap, less electron-hole recombination as well as a larger specific area (Fig. 4b). Therefore, the P/Ti molar ratio is selected as 0.04 in further reaction optimizations.

Table 1
The BET surface areas of pure TiO_2 and P-TiO_2.

Sample	S_{BET} (m^2/g)
TiO_2	98.2
P-TiO_2-0.04	144.3

The reaction pH plays an important role in the photodegradation rate of organic pollutants. The change of pH can affect the electrostatic repulsion between pollutants and catalyst surfaces by changing the surface charge and the chemical state of photocatalysts. As shown in Fig. 8b, the degradation efficiency of CIP increases from 27.4 % to 55.7 % with increasing pH from 3 to 7 and decreases when further increasing pH from 7 to 11. In general, the degradation efficiencies of CIP under acidic conditions are lower than those under alkaline conditions. We hypothesize that this is due to catalyst surface charge and the CIP molecular form. The isoelectric point of pure TiO_2 and P-TiO_2 (P/Ti = 0.04) was measured to be 5.79 and 5.1 respectively. The CIP molecular has 3 different forms at pKa values of 6.16 and 8.23, namely cation ($CIP^{0,+}$), amphoteric ($CIP^{-,+}$), and anion ($CIP^{-,0}$) [47]. Thus, CIP exists as the protonated form at pH 6.16. Under acidic conditions (pH = 3, 5), electrostatic repulsion between the surface of photocatalyst and the CIP molecule lowered the photocatalytic degradation. Meanwhile, the low degradation efficiency was attributed to the corrosion and decomposition of the catalystunder acidic conditions [48]. Under pH 7, the P-TiO_2 catalyst surface exhibits a negative charge, while the CIP exists as an amphoteric ion. This promotes electrostatic attraction between CIP and P-TiO_2, thus maximizing the degradation of CIP [49]. Therefore, further experiments were all carried out at pH 7.

We also discuss the effect of the initial CIP concentration on the kinetics of photocatalytic degradation. As shown in Fig. 8c, the photocatalytic degradation of CIP follows first-order kinetics under different initial pollutant concentrations. The rate constants for initial CIP concentrations of 5, 10, and 20 mg L^{-1} are calculated to be 7.3×10^{-3} min^{-1}, 2.9×10^{-3} min^{-1}, and 2.1×10^{-3} min^{-1}, respectively. When the initial concentration of CIP was 5 mg L^{-1}, the highest photodegradation efficiency of 72.49 % was achieved after 120 min. The CIP solution with lower initial concentration contains fewer CIP molecules. The higher CIP removal efficiency is attributed to the reduction of CIP molecules that react with the generated •OH radicals. By increasing the initial CIP concentration, the generated •OH radicals will react with more CIP molecules, leading to the decreased degradation efficiency. Further, the effect of the initial concentration on the removal efficiency of the CIP can also be explained by the integral form of the first-order reaction equation $-dC/dt = kC$, where k is the reaction rate constant shown in Fig. 8c and C is the concentration of the contaminant. As the reaction progressed, the concentration of CIP decreased. Therefore, in the same reaction period, the degradation efficiency decreases with the increasing initial CIP concentrations.

3.3. HC degradation of CIP

Inlet pressure plays a vital role in the HC process. It can significantly contribute to the duration of bubbles' existence, size, and •OH radical generation. The effect of inlet pressure in the range of 2–4 bar was used with an initial CIP concentration of 10 mg/L and pH = 7. Fig. 9 illustrates the influence of inlet pressure on CIP degradation. As the inlet pressure increases, the degradation of CIP first increases and then decreases. The optimized HC degradation of CIP appears at 3 bar. As operating pressure increases to the optimum value (3 bar), in the venturi throat, the number of cavities grows to a maximum, forming mature cavitation bubbles, which increase in density and prompt the hydrolysis of water molecules to produce high-intensity •OH. Meanwhile, the increase in fluid turbulence has also increased the effective utilization of •OH radicals, contributing to the higher degradation and faster degradation rate of CIP. However, when the inlet pressure is further increased to 4 bar, the degradation rate slows down and starts to decrease. This

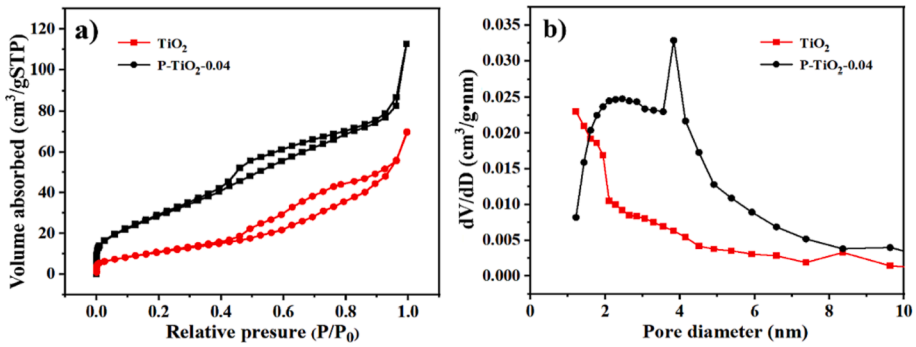

Fig. 7. (a) Typical N_2 adsorption/desorption isotherms and (b) BJH pore size distribution plots of pure TiO_2 and P-TiO_2-0.04.

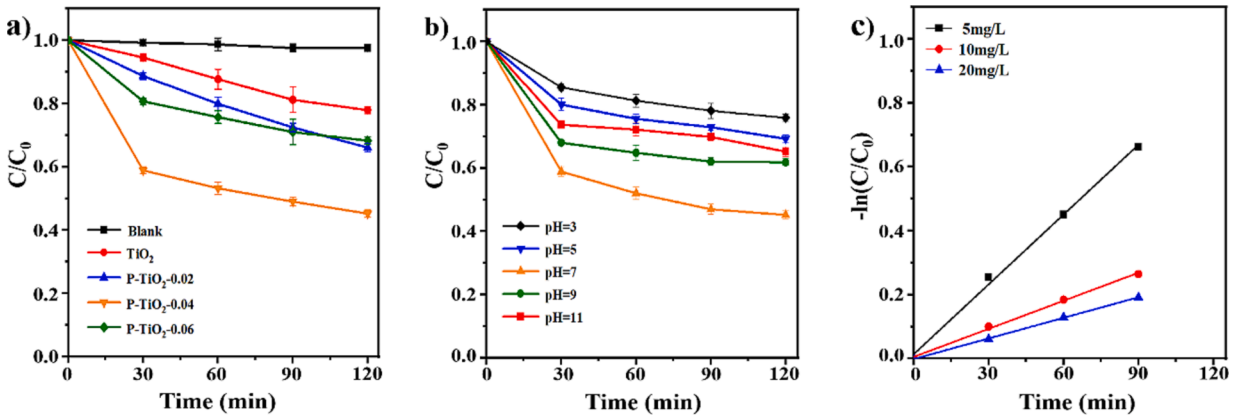

Fig. 8. Effect of (a) different P/Ti molar concentrations (under [photocatalyst] = 0.5 g L^{-1}, [CIP] = 10 mg L^{-1}, [pH] = 7), (b) pH (under [P-TiO_2-0.04] = 0.5 g L^{-1}, [CIP] = 10 mg L^{-1}) and (c) initial CIP concentrations on photocatalytic degradation of CIP (under [P-TiO_2-0.04] = 0.5 g L^{-1}, [pH] = 7).

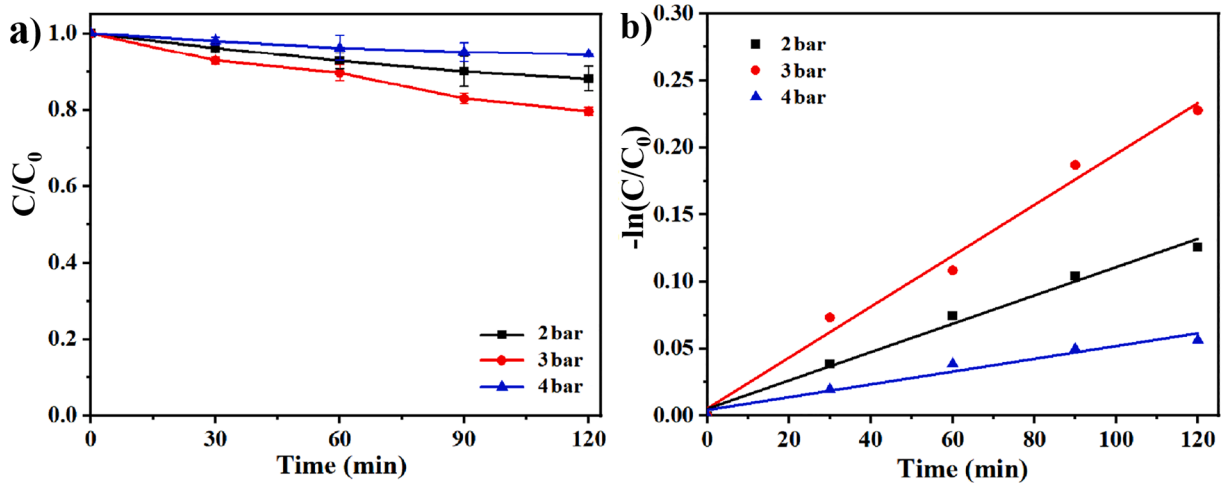

Fig. 9. Influence of the HC inlet pressure on (a) CIP removal efficiency and (b) degradation rate of CIP (under [P-TiO_2-0.04] = 0.5 g L^{-1}, [CIP] = 10 mg L^{-1}, [pH] = 7).

could be due to the occurrence of supercavitation. Under high inlet pressure, a big number of bubbles and cavity clouds formed. This could slow down the process of cavitation bubbles from growth to collapse, thus weakening the cavitation phenomenon [23]. Bagal et al. used venturi tubes to degrade DCF (Diclofenac) and obtained the highest degradation rate when the inlet pressure was 3 bar [33], similar to our results. Based on the above results, 3 bar was selected as the optimal inlet pressure in HC + photocatalytic degradation.

3.4. HC-assisted photocatalytic degradation of CIP

The degradation efficiencies and the corresponding kinetic constants of CIP under different advanced oxidation processes are shown in Fig. 10. The combination of HC and photocatalytic processes was investigated by comparing the performance of individual HC and UV processes with other HC-based AOPs. All the experiments were done using a CIP concentration of 10 mg L^{-1} and catalyst dose of 0.5 g L^{-1} at pH 7. For AOP involving UV irradiation, the light irradiation time was

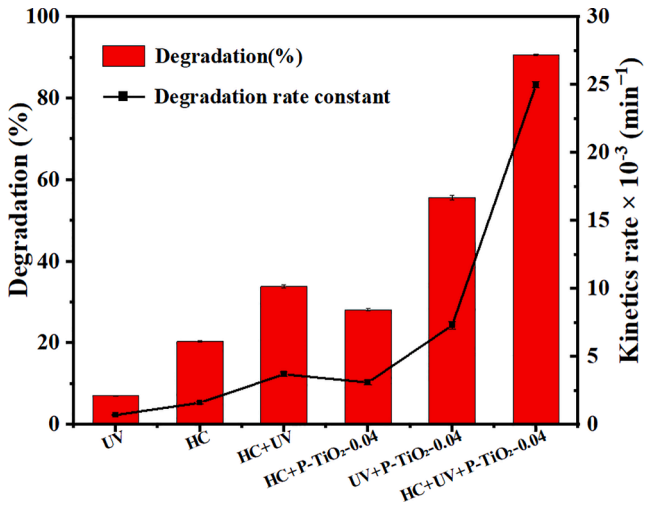

Fig. 10. Demonstration of degradation rate of CIP under different advanced oxidation processes (under [P-TiO_2-0.04] = 0.5 g L^{-1}, [CIP] = 10 mg L^{-1}, [pH] = 7).

120 min. Under the HC process, the removal efficiency of CIP was only 20.37 % with a rate constant of 0.0016 min^{-1}, while under the HC + UV process, the removal efficiency and rate constant of CIP were 33.9 % and 0.0037 min^{-1}, respectively. This indicates that HC may enhance the UV process by producing more radicals (Fig. 10). The HC-assisted photocatalytic process resulted in a maximum removal rate and a rate constant of 90.63 % and 0.025 min^{-1}. Compared to the simple photocatalytic process, the synergetic system shows higher CIP degradation. This may be due to the generation of interruptions and HC shear forces which rapidly clean the surface of the photocatalysts and transfer small molecular compounds. Thus, more active sites will be exposed to subsequent photocatalytic reactions. The addition of catalyst nanoparticles can also promote the production of cavitation bubbles and active substances through heterogeneous nucleation. Therefore, the presence of HC can improve the positive interaction that occurs between the CIP organic molecule and the generated free radical during photocatalysis, resulting in a degradation of CIP that is much higher under the HC + photocatalytic process than that under the individual HC and photocatalytic processes.

3.5. Stability and transformation of the available P-TiO_2-0.04 photocatalyst

In order to further discuss the role of HC in the photocatalytic degradation of CIP, we compared the microstructure of P-TiO_2-0.04 before and after synergy processes. Fig. 11a illustrates the XRD patterns of the available P-TiO_2-0.04 nanocatalyst after HC-assisted photocatalytic process. There are nearly no changes in diffraction peaks and positions of P-TiO_2-0.04 composites before and after CIP degradation, indicating that the P-TiO_2-0.04 remains stable after the HC-assisted photocatalytic reactions. Fig. 11b shows the typical N_2 adsorption/desorption isotherms of P-TiO_2-0.04 particles after reaction. Moreover, the sample showed a higher steepness of hysteresis, a wider hysteresis loop, and an obvious saturated adsorption platform. This indicated a higher order of mesoporosity, more mesopores, and an ordered pore structure after HC circulation agitation [50]. SEM was used to observe the morphology and particle morphology of P-TiO_2-0.04 nanoparticles before and after HC + photocatalysis processes (Fig. 11c and d). Particle distribution was shown to be more uniform and well dispersed. The surface was also smoother compared to the P-TiO_2-0.04 before the reaction.

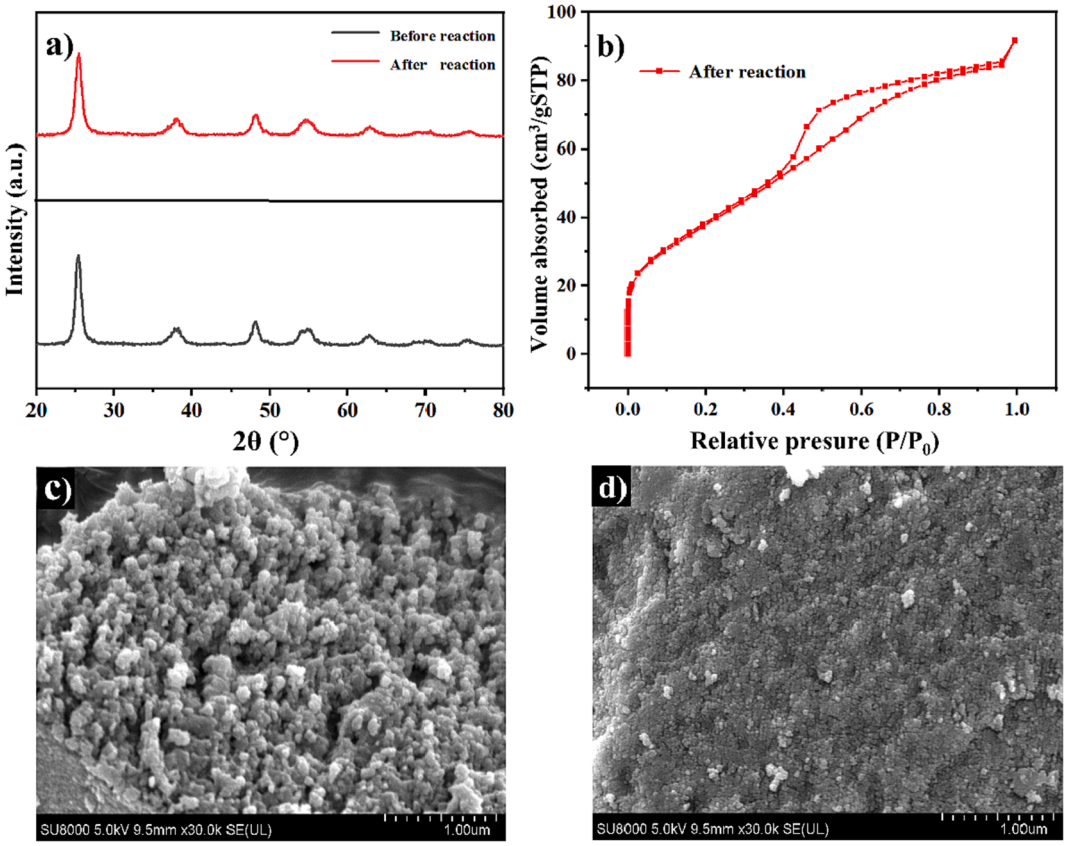

Fig. 11. (a) XRD patterns of P-TiO_2-0.04 nanocatalyst before and after reaction, (b) the typical nitrogen adsorption/desorption isotherms of P-TiO_2-0.04 particles after HC + photocatalytic treatment, (c) SEM image of P-TiO_2-0.04 nanoparticles before reaction and (d) SEM image of P-TiO_2-0.04 nanoparticles after reaction.

The BET surface area, pore size, and pore volume of untreated and treated P-TiO_2-0.04 particles are shown in Table 2. After the HC + photocatalytic process, the pore size of the catalyst sample reduced from 3.8 nm to 2.0 nm. The BET-specific surface area increased significantly from 113.1 m^2/g to 144.3 m^2/g and the pore volume increased from 0.1491 cm^3/g to 0.1742 cm^3/g. The pore structure can be better improved through the HC process and the mesoporous structure can also be retained under extreme HC conditions, resulting in a larger BET surface area. This is consistent with the results of the SEM morphology study. Based on the above results, we may deduce a synergy interaction between HC and photocatalysis in the CIP degradation process. Under HC treatment, extreme conditions such as high temperature and pressure caused by cavitation bubble collapse trigger microjets, shear forces, and turbulence that will wash and clean the photocatalyst surface and make the catalyst surface particles more evenly dispersed. As a result, more active sites are exposed on the catalyst surface, which can enhance the interaction activity between P-TiO_2-0.04 and organic macromolecules [29,30]. The HC process can also improve the pore microstructure of the photocatalysts. The increased area surface will promote the adsorption of CIP. Consequently, the degradation rate of CIP is considerably improved by the synergistic interaction between the HC and photocatalytic processes.

3.6. Detection of active substances generated in HC-assisted photocatalytic reaction

The radical species produced during the HC + photocatalytic process were studied by comparing the degradation rate of CIP under different trapping agents. Isopropanol (IPA), potassium iodide (KI), and 1,4-benzoquinone (BQ) were utilized for trapping hydroxyl radicals (•OH), holes (h^+), and superoxide radicals ($\bullet O_2^-$), respectively [51]. The addition of IPA, KI, and BQ suppressed the photocatalytic degradation of CIP to a certain extent, indicating that •OH, h^+, and $\bullet O_2^-$ all contributed to the degradation of CIP (Fig. 12a). Notably, the addition of KI most obviously inhibited CIP degradation suggesting that h^+ is the main reactive species during the HC-assisted photocatalytic process. It can be also observed that the degradation of CIP decreased to 58.5 % after the addition of IPA, indicating that the hydroxyl radical (•OH) is also an active species in removal of CIP. The addition of BQ slightly suppressed the photocatalytic degradation of CIP implying that $\bullet O_2^-$ does not play a very important role in the synergy. According to these results, h^+ is the leading radical and •OH performs a secondary important function in the HC + photocatalytic process of the CIP degradation.

EPR (Electron Paramagnetic Resonance) spectroscopy was used to detect and characterize the paramagnetic species in the photocatalytic reaction of materials. As shown in Fig. 12b, no distinctive characteristic signal was generated under darkness. This indicates that there is no generation of $\bullet O_2^-$ without light. The characteristic signals of six DMPO•O_2^- spin adducts can be observed after ten minutes of irradiation, indicating the production of $\bullet O_2^-$. Three strong signal peaks with intensity ratio 1:1:1 appeared under darkness (Fig. 12c). In addition, a significant decrease in the intensities of three signal peaks which indicated the generation of h^+ under irradiation could be observed. This is due to the ability of TEMPO to react with photogenerated holes, thus weakening the signal peak intensity. As shown in Fig. 12d, there is no EPR signal under darkness after adding DMPO. Whereas four significant signal peaks appeared with an intensity ratio of 1:2:2:1 after 10 min of irradiation. The intensity ratio of 1:2:2:1 is considered as a characteristic signal for DMPO•OH spin trapping. Thus, during the photocatalytic process, •OH can be produced by reaction between P-TiO_2-0.04 and water molecules. This confirmed that the active species h^+, •OH, and $\bullet O_2^-$ were generated under irradiation.

Table 2
N_2 adsorption–desorption results for the catalysts.

Sample	S_{BET} (m^2/g)	Pore size (nm)	Pore volume (cm^3/g)
Before reaction	113.1	3.8	0.1491
After reaction	144.3	2.0	0.1742

3.7. Possible mechanism and process of HC-assisted photocatalytic process for CIP degradation with P-TiO_2

Fig. 13 illustrates the potential mechanism of HC-assisted photocatalytic CIP decomposition in the presence of P-TiO_2 which can be summarized in two typical ways, hydrodynamic cavitation oxidation and catalytic oxidation [49,52].

Firstly extreme conditions such as high temperature (500–15000 K), high pressure (100–5000 atm), hot spots, cavitation luminescence, etc. can be generated. These extreme conditions contribute to the production of highly oxidizing radicals such as hydroxyl radicals (•OH). Among these highly oxidizing radicals, the •OH is directly involved in the cleavage of CIP (7). Furthermore, •OH and hydrogen radicals (•H) can also be formed by the decomposition of H_2O molecules during HC process (3). Subsequently, •H react with oxygen molecules dissolved in an aqueous solution causing the generation of superoxide radicals ($\bullet O_2^-$) (4). Finally, •OH are formed via a reaction involving superoxide radicals (5,6).

$$H_2O + \text{hot spot (HC effect)} \rightarrow \bullet H + \bullet OH \quad (3)$$

$$\bullet H + O_2 \rightarrow \bullet O_2^- + H^+ \quad (4)$$

$$\bullet O_2^- + H^+ \rightarrow HO_2 \quad (5)$$

$$HO_2 + H_2O \rightarrow H_2O_2 + \bullet OH \quad (6)$$

$$\bullet OH + CIP \rightarrow CO_2 + H_2O + F^- + NO_3^- \quad (7)$$

$$\bullet O_2^- + CIP \rightarrow CO_2 + H_2O + F^- + NO_3^- \quad (8)$$

Wide-wavelength range light can excite the semiconductor catalyst P-TiO_2 to generate holes (h^+) which can directly decompose CIP adsorbed on the catalyst surface (12). The addition of solid catalysts can also produce more cavitation bubbles in HC process. Under the HC effect, the catalyst surface can retain a clean state, provide sufficient active sites, and be exposed to light for longer times [29,30]. Meanwhile, the excitation of the semiconductor catalyst under UV light produces electrons (e^-) on the conduction band (CB) and holes (h^+) on the valence band (VB) of P-TiO_2 (10). The CIP molecules can be directly degraded by superoxide radicals ($\bullet O_2^-$) (8), which are generated by the combination of electrons (e^-) and oxygen molecules (13). Subsequently, the $\bullet O_2^-$ reacts with H^+ and H_2O molecules to produce hydrogen peroxide (H_2O_2) (14). The H_2O_2 can produce more •OH for the degradation of CIP (15). The H_2O molecules can directly react with the holes (h^+) producing •OH (11). The holes (h^+) can also directly participate in the reaction of the CIP degradation [53] (12). The reactive species (•OH and h^+) formed during the reaction can effectively degrade CIP molecules.

$$P\text{-}TiO_2 + \text{light (HC effect)} \rightarrow P\text{-}TiO_2{}^* \quad (9)$$

$$P\text{-}TiO_2{}^* \rightarrow h^+ (VB) + e^- (CB) \quad (10)$$

$$h^+ (VB) + H_2O \rightarrow \bullet OH + H^+ \quad (11)$$

$$h^+ (VB) + CIP \rightarrow CO_2 + H_2O + F^- + NO_3^- \quad (12)$$

$$e^- (CB) + O_2 \rightarrow \bullet O_2^- \quad (13)$$

$$\bullet O_2^- + H_2O + H^+ \rightarrow H_2O_2 + O_2 \quad (14)$$

$$H_2O_2 \rightarrow 2\bullet OH \quad (15)$$

$$\bullet OH + CIP \rightarrow CO_2 + H_2O + F^- + NO_3^- \quad (16)$$

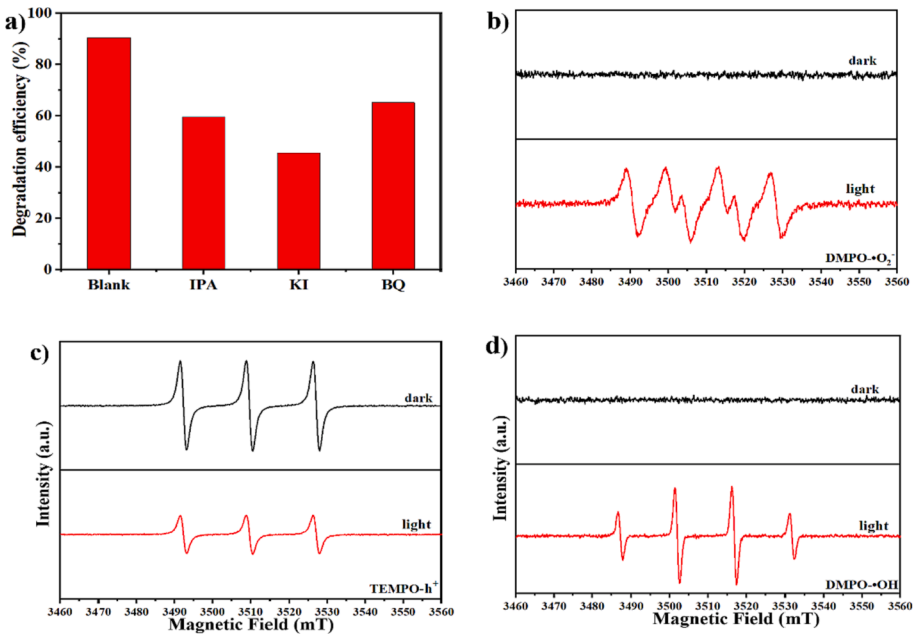

Fig. 12. Effects of trapping agents on HC-assisted photocatalytic degradation of CIP caused by P-TiO_2-0.04 (a) and EPR spectra for (b) DMPO-•O_2^- (c) TEMPO-h^+ and (d) DMPO-•OH.

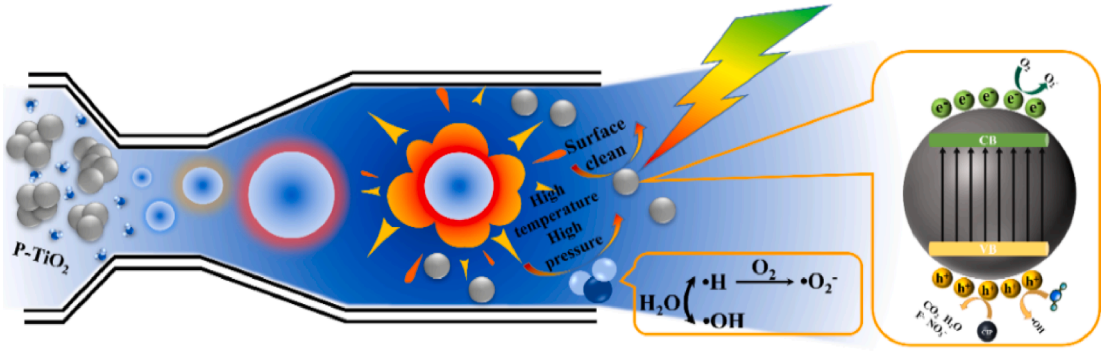

Fig. 13. The possible mechanism of HC-assisted photocatalytic process with the addition of P-TiO_2.

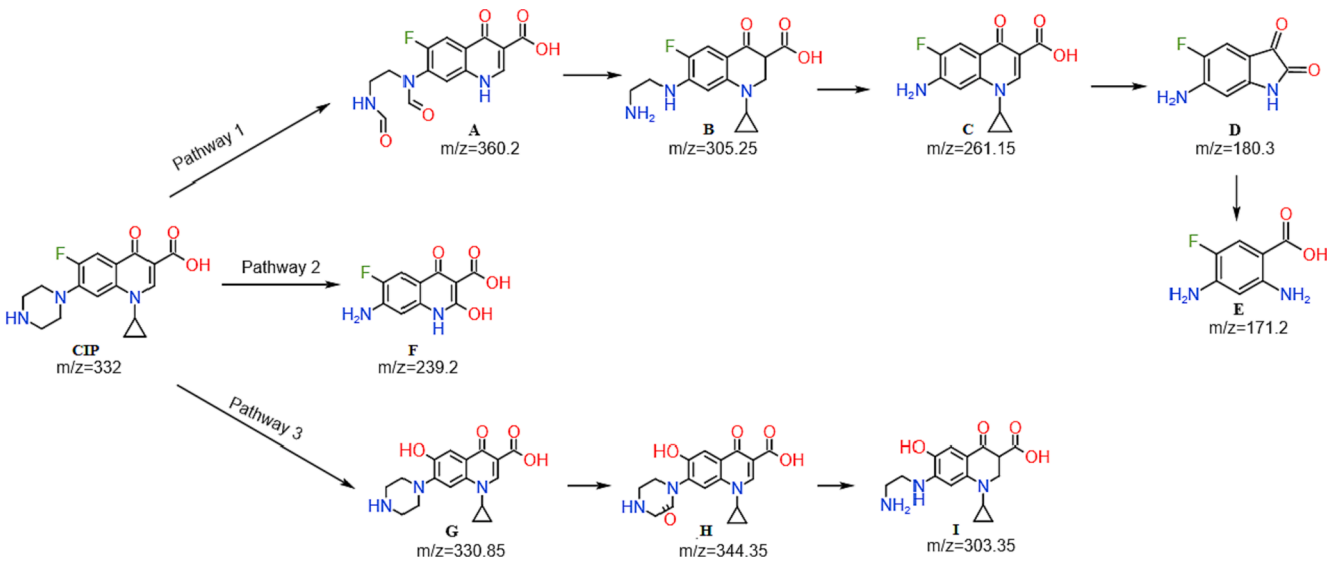

Fig. 14. Proposed degradation pathways of CIP by the HC-assisted photocatalytic hybrid advanced oxidation degradation process.

3.8. Identification of by-products and degradation pathways

The decomposition pathways of CIP were studied by detecting intermediate products using LC-MS analysis. The structures of the by-products indicate that the photocatalytic and HC + photocatalytic decomposition of CIP can happen through three typical pathways (Fig. 14). In Pathway 1, the CIP molecules are decomposed to a dialdehyde derivative A (*m/z* of 362) through the oxidization of the piperazine chain and the opening relations. This can be attributed to the attacking of h^+ causing the oxidization of the piperazine chain [54]. The formation of intermediate B (*m/z* of 305.25) is attributed to the decarbonylation of intermediate A via losing two aldehyde groups. Next, intermediate B loses a secondary amine nitrogen and formaldehyde from the amine side chain and forms intermediate C (*m/z* of 261.5) [55]. Due to the h^+/•OH attack, the ring structure opens to remove the quinolone moiety of C, and then closes as a five-membered ring. Intermediate D (*m/z* of 180.3) is generated via this process [56]. Intermediate E (*m/z* of 171.2) is formed through the opening of the five-membered ring and the removal of the lateral groups of intermediate D. M. Salari et al. also reported the structure of intermediate E [57]. Finally, the CIP molecules are almost completely destroyed. Pathway 2 follows a route of CIP → F (*m/z* = 239.2) based on the oxidation of the cyclopropyl group and cleavage of the ring structure. The CIP molecule first gains an H_2O molecule, loses a piperazine ring and a C_3H_4, and forms intermediate F with *m/z* 239.2 [47]. In pathway 3, intermediate G (*m/z* = 330.85) is generated by substitution on the quinolone molecule of CIP, which was previously reported to be produced by a molecule attack on the F-atom [58]. Intermediate H with a ketone group (*m/z* = 344.35) is formed due to the loss of O and H atoms of the piperazine group (*m/z* = 344.35) from intermediate G. The oxidation of the CIP molecule contributes to the C═O group introduced into the piperazinyl substitution The F atom is then replaced by hydroxyl on the ring of the quinolone moiety. Subsequently, intermediate H loses C_2H_2O, leading to the formation of intermediate I [55].

The experiment did not achieve complete mineralization of the CIP at the end of the experiment. It was previously found that the luminescent decay of the marine bacterium V. fischeri could be able to determine the toxicity of by-products [58]. All of the by-products in Fig. 14 have negligible or no antimicrobial toxicity compared to the CIP parent molecule [59]. The treated water samples were determined to be non-toxic. Therefore, HC-assisted photocatalytic processes can solve the problem of CIP removal from sewage.

4. Conclusions

In this study, a hybrid advanced oxidation degradation reactor was built on the basis of combining HC and photocatalysis techniques. Individual HC, photocatalytic, and HC-assisted photocatalytic removal efficiency of CIP were studied with the addition of P-doped TiO_2. Nanoparticles of P-TiO_2 with an optimal P/Ti ratio of 0.04 were synthesized by a sol–gel method. The optimal reaction conditions were determined as photocatalyst amount of 0.5 g L^{-1}, initial pH value of 7, CIP concentration of 10 mg L^{-1}, and operating pressure of 3 bar. The highest CIP removal ratio reached 90.63 % in the HC + P-TiO_2-0.04 + light system within 120 min, which is significantly higher than the 20.37 % in HC and 55.7 % in P-TiO_2-0.04 + light systems. The synergetic effect between hydrodynamic cavitation (HC) and photocatalysis would make the particle size of P-TiO_2-0.04 nano photocatalysts smaller with improved dispersion, inducing more active sites and a larger surface area. The microstructural modification enhanced the ciprofloxacin degradation and the cleaner catalyst surface retained by microjets improves the sustainability of photocatalyst. Moreover, three different types of free radicals (h^+, •OH, and $•O_2^-$) were identified to be involved in the CIP degradation during the hybrid HC-assisted photocatalytic process, while three possible removal routes were also proposed. Overall, the hybrid system of HC + photocatalysis may become a potential technique available for the treatment of antibiotic effluents in large quantities.

CRediT authorship contribution statement

Mengfan Chen: Methodology, Investigation, Formal analysis, Data curation, Writing – original draft. **Kai Zhuang:** Investigation, Resources. **Jiayi Sui:** Investigation, Data curation. **Congting Sun:** Methodology, Supervision, Writing – review & editing. **Youtao Song:** Funding acquisition, Supervision. **Nanxun Jin:** Investigation.

Declaration of Competing Interest

The authors declare that they have no known competing financial interests or personal relationships that could have appeared to influence the work reported in this paper.

Data availability

No data was used for the research described in the article.

Acknowledgments

This work was financially supported by the National Natural Science Foundation of China (No. 41977205), the Natural Science Foundation of Liaoning Province (2021-MS-152), and the Key research project of Liaoning Provincial Department of Education (LZD202004).

Appendix A. Supplementary data

Supplementary data to this article can be found online at https://doi.org/10.1016/j.ultsonch.2022.106265.

References

[1] Y.J. Ben, C.X. Fu, M. Hu, L. Liu, M.H. Wong, C.M. Zheng, Human health risk assessment of antibiotic resistance associated with antibiotic residues in the environment: A review, Environ. Res. 169 (2019) 483–493.
[2] M. Conde-Cid, A. Nunez-Delgado, M.J. Fernandez-Sanjurjo, E. Alvarez-Rodriguez, D. Fernandez-Calvino, M. Arias-Estevez, Tetracycline and Sulfonamide Antibiotics in Soils: Presence, Fate and Environmental Risks, Processes 8 (2020) 1479.
[3] W. Gwenzi, Z. Shamsizadeh, S. Gholipour, M. Nikaeen, The air-borne antibiotic resistome: Occurrence, health risks, and future directions, Sci. Total Environ. 804 (2022), 150154.
[4] J. O'Neill. Tackling drug-resistant infections globally: final report and recommendations, 2016. https://apo.org.au/node/63983. (Accessed 15 June 2021).
[5] J.L. Wang, R. Zhuan, Degradation of antibiotics by advanced oxidation processes: An overview, Sci. Total Environ. 701 (2020), 135023.
[6] Y.F. Han, L.Y. Yang, X.M. Chen, Y. Cai, X.Y. Zhang, M.C. Qian, X.K. Chen, H. H. Zhao, M. Sheng, G.M. Cao, G.X. Shen, Removal of veterinary antibiotics from swine wastewater using anaerobic and aerobic biodegradation, Sci. Total Environ. 709 (2020), 136094.
[7] A. Mohammad, M.E. Khan, M.H. Cho, T. Yoon, Adsorption promoted visible-light-induced photocatalytic degradation of antibiotic tetracycline by tin oxide/cerium oxide nanocomposite, Appl. Surf. Sci. 565 (2021), 150337.
[8] F. Wang, Y.C. Zhang, H. Ming, L. Wang, Z.Y. Zhao, Y.H. Wang, J.Y. Liang, Y. Qin, Degradation of the ciprofloxacin antibiotic by photo-Fenton reaction using a Nafion/iron membrane: role of hydroxyl radicals, Environ. Chem. Lett. 18 (2020) 1745–1752.
[9] C. Diaz-Quiroz, L. Gonzalez, M.S. Alvarez, J.F. Hernandez-Chavez, A. Rodriguez, F. J. Deive, G. Ulloa-Mercado, Biocompatible amino acid-based ionic liquids for extracting hormones and antibiotics from swine effluents, Sep. Purif. Technol. 250 (2020) 11706.
[10] M. Verma, A.K. Haritash, Review of advanced oxidation processes (AOPs) for treatment of pharmaceutical wastewater, Adv. Environ. Res.-Int. J. 9 (2020) 1–17.
[11] S. Peiris, H.B. de Silva, K.N. Ranasinghe, S.V. Bandara, I.R. Perera, Recent development and future prospects of TiO_2 photocatalysis, J. Chin. Chem. Soc. 68 (2021) 738–769.
[12] D.J. Chen, Y.L. Cheng, N. Zhou, P. Chen, Y.P. Wang, K. Li, S.H. Huo, P.F. Cheng, P. Peng, R.C. Zhang, L. Wang, H. Liu, Y.H. Liu, R. Ruan, Photocatalytic degradation of organic pollutants using TiO_2-based photocatalysts: A review, J. Cleaner Prod. 268 (2020), 121725.

[13] A. Mittal, B. Mari, S. Sharma, V. Kumari, S. Maken, K. Kumari, N. Kumar, Non-metal modified TiO_2: a step towards visible light photocatalysis, J. Mater. Sci. - Mater. Electron. 30 (2019) 3186–3207.

[14] S.Y. Mendiola-Alvarez, M.A. Hernandez-Ramirez, J.L. Guzman-Mar, L.L. Garza-Tovar, L. Hinojosa-Reyes, Phosphorous-doped TiO_2 nanoparticles: synthesis, characterization, and visible photocatalytic evaluation on sulfamethazine degradation, Environ. Sci. Pollut. Res. Int. 26 (2019) 4180–4191.

[15] H.J. Feng, M.H. Zhang, L.E. Yu, Phosphorus-Doped TiO_2 Catalysts with Stable Anatase-Brookite Biphase Structure: Synthesis and Photocatalytic Performance, J. Nanosci. Nanotechnol. 13 (2013) 4981–4989.

[16] L.G. Devi, R. Kavitha, A review on non metal ion doped titania for the photocatalytic degradation of organic pollutants under UV/solar light: Role of photogenerated charge carrier dynamics in enhancing the activity, Appl. Catal., B 140–141 (2013) 559–587.

[17] J.A. Khan, C. Han, N.S. Shah, H.M. Khan, M.N. Nadagouda, V. Likodimos, P. Falaras, K. O'Shea, D.D. Dionysiou, Ultraviolet-Visible Light–Sensitive High Surface Area Phosphorous-Fluorine–Co-Doped TiO_2 Nanoparticles for the Degradation of Atrazine in Water, Environ. Eng. Sci. 31 (2014) 435–446.

[18] X. Wang, J. Jia, Y. Wang, Combination of photocatalysis with hydrodynamic cavitation for degradation of tetracycline, Chem. Eng. J. 315 (2017) 274–282.

[19] P.R. Gogate, Improvements in Catalyst Synthesis and Photocatalytic Oxidation Processing Based on the Use of Ultrasound, Top. Curr. Chem. (Cham) 378 (2020) 29.

[20] P. Thanekar, N.J. Lakshmi, M. Shah, P.R. Gogate, Z. Znak, Y. Sukhatskiy, R. Mnykh, Degradation of dimethoate using combined approaches based on hydrodynamic cavitation and advanced oxidation processes, Process Saf. Environ. Prot. 143 (2020) 222–230.

[21] P. Wu, L. Bai, W. Lin, On the definition of cavitation intensity, Ultrason. Sonochem. 67 (2020), 105141.

[22] Z. Xu, K. Yasuda, S. Koda, Numerical simulation of liquid velocity distribution in a sonochemical reactor, Ultrason. Sonochem. 20 (2013) 452–459.

[23] B. Wang, H. Su, B. Zhang, Hydrodynamic cavitation as a promising route for wastewater treatment – A review, Chem. Eng. J. 412 (2021), 128685.

[24] Z.-Y. Dong, K. Zhang, R.-H. Yao, Degradation of refractory pollutants by hydrodynamic cavitation: Key parameters to degradation rates, J. Hydrodyn. 31 (2018) 848–856.

[25] S. Das, A.P. Bhat, P.R. Gogate, Degradation of dyes using hydrodynamic cavitation: Process overview and cost estimation, J. Hydrodyn. 42 (2021), 102126.

[26] K. Roy, V.S. Moholkar, Mechanistic analysis of carbamazepine degradation in hybrid advanced oxidation process of hydrodynamic cavitation/UV/persulfate in the presence of $ZnO/ZnFe_2O_4$, Sep. Purif. Technol. 270 (2021), 118764.

[27] Z. Xu, C.Y. Ma, J.Y. Xu, X.J. Liu, Dynamical properties of iodine release in potassium iodide solution under combination of ultrasound and light irradiations, Ultrason. Sonochem. 16 (2009) 475–480.

[28] P. Wu, L. Bai, W. Lin, X. Wang, Mechanism and dynamics of hydrodynamic-acoustic cavitation (HAC), Ultrason. Sonochem. 49 (2018) 89–96.

[29] S. Rajoriya, S. Bargole, S. George, V.K. Saharan, P.R. Gogate, A.B. Pandit, Synthesis and characterization of samarium and nitrogen doped TiO_2 photocatalysts for photo-degradation of 4-acetamidophenol in combination with hydrodynamic and acoustic cavitation, Sep. Purif. Technol. 209 (2019) 254–269.

[30] D. Panda, S. Manickam, Hydrodynamic cavitation assisted degradation of persistent endocrine-disrupting organochlorine pesticide Dicofol: Optimization of operating parameters and investigations on the mechanism of intensification, Ultrason. Sonochem. 51 (2019) 526–532.

[31] S.D. Hyman, J.W. Lazio, N.E. Kassim, P.S. Ray, C.B. Markwardt, F. Yusef-Zadeh, A powerful bursting radio source towards the Galactic Centre, Nature. 434 (2005) 50–52.

[32] G. Li, L. Yi, J. Wang, Y. Song, Hydrodynamic cavitation degradation of Rhodamine B assisted by $Fe^{(3+)}$-doped TiO_2: Mechanisms, geometric and operation parameters, Ultrason. Sonochem. 60 (2020), 104806.

[33] M.V. Bagal, P.R. Gogate, Degradation of diclofenac sodium using combined processes based on hydrodynamic cavitation and heterogeneous photocatalysis, Ultrason. Sonochem. 21 (2014) 1035–1043.

[34] L. Lin, R.Y. Zheng, J.L. Xie, Y.X. Zhu, Y.C. Xie, Synthesis and characterization of phosphor and nitrogen co-doped Titania, Appl. Catal., B. 76 (2007) 196–202.

[35] Z. Zhang, C. Zhao, Y. Duan, C. Wang, Z. Zhao, H. Wang, Y. Gao, Phosphorus-doped TiO_2 for visible light-driven oxidative coupling of benzyl amines and photodegradation of phenol, Appl. Surf. Sci. 527 (2020), 146693.

[36] X. Bai, J. Jia, Y. Du, X. Hu, J. Li, E. Liu, J. Fan, Multi-level trapped electrons system in enhancing photocatalytic activity of TiO_2 nanosheets for simultaneous reduction of Cr (VI) and RhB degradation, Appl. Surf. Sci. 503 (2020), 144298.

[37] J. Niu, P. Lu, M. Kang, K. Deng, B. Yao, X. Yu, Q. Zhang, P-doped TiO_2 with superior visible-light activity prepared by rapid microwave hydrothermal method, Appl. Surf. Sci. 319 (2014) 99–106.

[38] S. Landi, I.R. Segundo, E. Freitas, M. Vasilevskiy, J. Carneiro, C.J. Tavares, Use and misuse of the Kubelka-Munk function to obtain the band gap energy from diffuse reflectance measurements, Solid State Commun. 341 (2022), 114573.

[39] Z. Sun, V.F. Pichugin, K.E. Evdokimov, M.E. Konishchev, M.S. Syrtanov, V. N. Kudiiarov, K. Li, S.I. Tverdokhlebov, Effect of nitrogen-doping and post annealing on wettability and band gap energy of TiO_2 thin film, Appl. Surf. Sci. 500 (2020), 144048.

[40] L. Xu, C.-Q. Tang, J. Qian, Z.-B. Huang, Theoretical and experimental study on the electronic structure and optical absorption properties of P-doped TiO_2, Appl. Surf. Sci. 256 (2010) 2668–2671.

[41] X. Feng, P. Wang, J. Hou, J. Qian, Y. Ao, C. Wang, Significantly enhanced visible light photocatalytic efficiency of phosphorus doped TiO2 with surface oxygen vacancies for ciprofloxacin degradation: Synergistic effect and intermediates analysis, J. Hazard. Mater. 351 (2018) 196–205.

[42] S.A. Alim, T.S. Rao, S.R. Miditana, K.V.D. Lakshmi, Efficient and recyclable visible light-active nickel–phosphorus co-doped TiO_2 nanocatalysts for the abatement of methylene blue dye, J. Nanostruct. Chem. 10 (2020) 211–226.

[43] M.M. Rahman, A.Z. Shafiullah, A. Pal, M.A. Islam, I. Jahan, B.B. Saha, Study on Optimum IUPAC Adsorption Isotherm Models Employing Sensitivity of Parameters for Rigorous Adsorption System Performance Evaluation, Energies. 14 (2021) 7478.

[44] Y.J. Fangfei Li, M. Xia, M. Sun, B. Xue, D. Liu, X. Zhang, Effect of the P/Ti Ratio on the Visible-Light Photocatalytic Activity of P-Doped TiO_2, J. Phys. Chem. C. 113 (2009) 18134–18141.

[45] H. Kamisaka, K. Yamashita, Theoretical Study of the Interstitial Oxygen Atom in Anatase and Rutile TiO2: Electron Trapping and Elongation of the r(O−O) Bond, J. Phys. Chem. C. 115 (2011) 8265–8273.

[46] Y. Peng, J. He, Q. Liu, Z. Sun, W. Yan, Z. Pan, Y. Wu, S. Liang, W. Cheng, S. Wei, Impurity Concentration Dependence of Optical Absorption for Phosphorus-Doped Anatase TiO_2, J. Phys. Chem. C. 115 (2011) 8184–8188.

[47] K. Hu, R. Li, C. Ye, A. Wang, W. Wei, D. Hu, R. Qiu, K. Yan, Facile synthesis of Z-scheme composite of TiO_2 nanorod/g-C_3N_4 nanosheet efficient for photocatalytic degradation of ciprofloxacin, J. Cleaner Prod. 253 (2020), 120055.

[48] A. Hassani, A. Khataee, S. Karaca, Photocatalytic degradation of ciprofloxacin by synthesized TiO_2 nanoparticles on montmorillonite: Effect of operation parameters and artificial neural network modeling, J. Mol. Catal. A-Chem. 409 (2015) 149–161.

[49] A.V. Karim, A. Shriwastav, Degradation of ciprofloxacin using photo, sono, and sonophotocatalytic oxidation with visible light and low-frequency ultrasound: Degradation kinetics and pathways, Chem. Eng. J. 392 (2020), 124853.

[50] Václav Stengl, Snejana Bakardjieva, Molybdenum-Doped Anatase and Its Extraordinary Photocatalytic Activity in the Degradation of Orange II in the UV and vis Regions, J. Phys. Chem. C 114 (2010) 19308–19317.

[51] Z. Khan, S.A. Al-Thabaiti, Green synthesis of zero-valent Fe-nanoparticles: Catalytic degradation of rhodamine B, interactions with bovine serum albumin and their enhanced antimicrobial activities, J. Photochem. Photobiol. B 180 (2018) 259–267.

[52] C. Meng, M. Meng, X. Sun, C. Gu, H. Zou, X. Li, Rapid Degradation of Chlortetracycline Using Hydrodynamic Cavitation with Hydrogen Peroxide, Int. J. Environ. Res. Public. Health 19 (2022) 4167.

[53] M. El-Kemary, H. El-Shamy, I. El-Mehasseb, Photocatalytic degradation of ciprofloxacin drug in water using ZnO nanoparticles, J. Lumin. 130 (2010) 2327–2331.

[54] F. Chen, Q. Yang, Y. Wang, F. Yao, Y. Ma, X. Huang, X. Li, D. Wang, G. Zeng, H. Yu, Efficient construction of bismuth vanadate-based Z-scheme photocatalyst for simultaneous Cr(VI) reduction and ciprofloxacin oxidation under visible light: Kinetics, degradation pathways and mechanism, Chem. Eng. J. 348 (2018) 157–170.

[55] H.G. Guo, N.Y. Gao, W.H. Chu, L. Li, Y.J. Zhang, J.S. Gu, Y.L. Gu, Photochemical degradation of ciprofloxacin in UV and UV/H_2O_2 process: kinetics, parameters, and products, Environ. Sci. Pollut. Res. Int. 20 (2013) 3202–3213.

[56] X. Yu, J. Zhang, J. Zhang, J. Niu, J. Zhao, Y. Wei, B. Yao, Photocatalytic degradation of ciprofloxacin using Zn-doped Cu_2O particles: Analysis of degradation pathways and intermediates, Chem. Eng. J. 374 (2019) 316–327.

[57] M. Salari, G.R. Rakhshandehroo, M.R. Nikoo, Degradation of ciprofloxacin antibiotic by Homogeneous Fenton oxidation: Hybrid AHP-PROMETHEE method, optimization, biodegradability improvement and identification of oxidized by-products, Chemosphere 206 (2018) 157–167.

[58] J.C. Durán-Álvarez, E. Avella, R.M. Ramírez-Zamora, R. Zanella, Photocatalytic degradation of ciprofloxacin using mono- (Au, Ag and Cu) and bi- (Au–Ag and Au–Cu) metallic nanoparticles supported on TiO_2 under UV-C and simulated sunlight, Catal. Today 266 (2016) 175–187.

[59] T. Paul, M.C. Dodd, T.J. Strathmann, Photolytic and photocatalytic decomposition of aqueous ciprofloxacin: transformation products and residual antibacterial activity, Water Res. 44 (2010) 3121–3132.